

Article

Designing a Real-Time Implementable Optimal Adaptive Cruise Control for Improving Battery Health and Energy Consumption in EVs through V2V Communication

Carlo Fiorillo ¹, Mattia Mauro ¹, Atriya Biswas ^{2,*} , Angelo Bonfitto ¹  and Ali Emadi ²

¹ Department of Mechanical and Aerospace Engineering, Center for Automotive Research and Sustainable Mobility (CARS), Politecnico di Torino, 10129 Torino, Italy; fiorillocarlo.99@gmail.com (C.F.); s298497@studenti.polito.it (M.M.); angelo.bonfitto@polito.it (A.B.)

² McMaster Automotive Resource Center, McMaster University, Hamilt, ON L8P0A6, Canada; emadi@mcmaster.ca

* Correspondence: biswaa4@mcmaster.ca

Abstract: Battery electric vehicles (BEVs) face challenges like their limited all-electric range, the discrepancy between promised and actual energy efficiency, and battery health degradation, despite their environmental benefits. This article proposes an optimal adaptive cruise control (OACC) framework by leveraging ideal vehicle-to-vehicle communication to address these challenges. In a connected vehicle environment, where it is assumed that the *Ego* vehicle's vehicle control unit (VCU) accurately knows the speed and position of the *Leading* vehicle, the VCU can optimally plan the acceleration trajectory for a short-term future time window through a model predictive control (MPC) framework tailored to BEVs. The primary objective of the OACC is to reduce the energy consumption and battery state-of-health degradation of a BEV. The Chevrolet Spark 2015 is chosen as the BEV platform used to validate the effectiveness of the proposed OACC. Simulations conducted under urban and highway driving conditions, as well as under communication delay and infused noise, resulted in up to a 3.7% reduction in energy consumption and a 9.7% reduction in battery state-of-health (SOH) degradation, demonstrating the effectiveness and robustness of the proposed OACC.

Keywords: battery electric vehicles; battery state of health degradation; optimal speed trajectory planning; eco-driving; energy consumption; V2V communication



Citation: Fiorillo, C.; Mauro, M.; Biswas, A.; Bonfitto, A.; Emadi, A. Designing a Real-Time Implementable Optimal Adaptive Cruise Control for Improving Battery Health and Energy Consumption in EVs through V2V Communication. *Energies* **2024**, *17*, 1986. <https://doi.org/10.3390/en17091986>

Academic Editors: Massimo Guarnieri and Fangming Jiang

Received: 20 February 2024

Revised: 25 March 2024

Accepted: 17 April 2024

Published: 23 April 2024



Copyright: © 2024 by the authors. Licensee MDPI, Basel, Switzerland. This article is an open access article distributed under the terms and conditions of the Creative Commons Attribution (CC BY) license (<https://creativecommons.org/licenses/by/4.0/>).

1. Introduction

One of the biggest challenges, and simultaneously one of the biggest opportunities, in this era is in the area of energy and sustainability, and the transportation sector is sitting at the heart of it. Our current transportation sector is heavily dependent on fossil fuels. Nearly 88% of roughly 1.5 billion vehicles run on fossil fuels worldwide. The transport sector alone contributes significantly to global greenhouse gas (GHG) emissions [1], accounting for 21.6% of total anthropogenic emissions. Road transport is a significant contributor to this sector, responsible for 77.9% of the total CO₂ emissions associated with transportation. Supposing we want to move towards achieving net-zero emissions, powertrain electrification must be prioritized since electric vehicles (EVs) have been at the forefront of reducing GHG emissions in the current decade. Even if EVs consume electricity from fossil fuels, they are a better alternative to fossil fuel-fed vehicles because the carbon from power plant exhaust is more accessible for capture than carbon from the tailpipe of vehicles.

While the automotive industry is navigating towards electrification, recent trends suggest that EV sales have faced headwinds in some regions despite the enthusiasm for a green future. It is not being said that EV sales are not growing, but rather they are growing at a slower rate than expected, especially in the United States, as shown in Figure 1 [2,3].

Figure 1 depicts the recent trend in EV adoption rate in the primary EV markets and across the world.

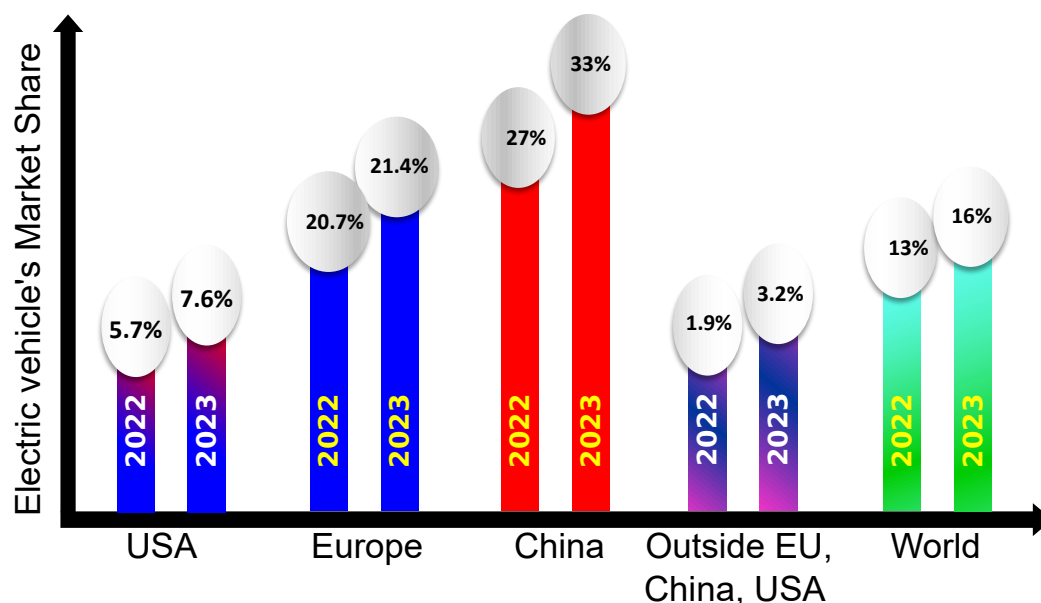


Figure 1. Comparison of EV sales across the world in the last two years with special attention given to the USA, China, Europe, and rest of the world [2].

Recent trends suggest a slow adoption of EVs even though the battery costs and average EV costs are declining [2,4] due to research and development on multiple fronts, including but not limited to artificial intelligence (AI)- and machine learning (ML)-based optimal battery material finding and battery design [5], AI- and ML-based optimal powertrain configuration design and sizing [6,7], and cost-effective and digitalized vehicle development programs for EVs [8]. Three primary factors contribute to this slow adoption rate and apathy towards EVs:

- Limited all-electric range and reduced energy efficiency of electric powertrains;
- Deterioration of battery SOH before promised years of operation;
- Lack of widespread and reliable charging infrastructure.

Several studies that have been conducted to identify the root cause of the first two factors reveal that existing and prospective EV buyers find that their EV's battery reaches its end-of-life (EOL) long before what was promised to them. Similarly, EV users find discrepancies between the promised and actual all-electric ranges in real-world driving. It has been largely proven that many real-world factors, such as trip distance, ambient temperature, charging level, and driving behavior, affect the energy efficiency of the powertrain, resulting in discrepancies between the all-electric driving range promised by the original equipment manufacturers (OEMs) and real-world driving range [9]. Similarly, deviations between real-world battery EOL and promised EOL are inevitable due to many real-world and user-related factors, such as driving patterns, temperature, types of charging, and the energy management controller of the EV [10]. Typically, large-capacity EV batteries reach their EOL when their maximum capacity in terms of Ampere-hours (Ah) falls below 80–70% of their initial capacity [11]. In contrast, smaller-capacity batteries reach their EOL when their maximum available power falls below 80% of their initial maximum power [11].

Since there is an inevitable gap between EV testing conditions based on which the OEMs obtain their sticker values and government certifications and real-world EV operating conditions, and since the repercussions due to such gaps in terms of deterioration of energy efficiency and battery SOH cannot be alleviated with hardware-based improvements, software-level interventions in the VCU, especially in the energy management system (EMS), have been prioritized in both industry and academia. Unlike the EMSs for

hybrid electric vehicles (HEVs) or fuel-cell electric vehicles (FCEVs), the EMSs for EVs do not have the flexibility of delegating a portion of the tractive power requested to onboard power sources other than the battery. Consequently, they must ask the battery for whatever power the driver requests. Hence, the EMSs for EVs should be designed intelligently to avoid using the battery abusively, improving energy efficiency and battery SOH.

Due to such constraints of the EMSs of EVs, a few indirect approaches are prescribed in the literature. Among various possible avenues, one involves implementing an intelligent battery management system (BMS) to oversee and regulate the SOH degradation of every battery cell within the pack [12]. This approach maintains uniform capacity fading across all cells and prevents abnormal increases in capacity loss within any specific cell. Other strategies, such as charging and auxiliary power management, also allow for reduced charging times and an extended battery life cycle [13]. However, these two approaches need to take the aspect of real-world driving into account when designing an intelligent EMS-based VCU. Therefore, the authors of this article have shifted their focus to leveraging vehicle-to-vehicle (V2V) communications during real-world driving to incorporate an intelligent feature into the VCU through which the VCU can reduce the battery's SOH degradation and powertrain energy consumption. This feature is also quite well-known as an eco-driving feature, where the vehicles' speed trajectory is optimized given that there are other constraints such as maintaining a safe distance between vehicles, adhering to signals at intersections and speed limits of the road, and respecting the feasible limits of the powertrain components [14]. Moreover, this approach aligns with the contemporary automotive trend, emphasizing connected and autonomous vehicle technologies, specifically targeting enhanced energy efficiency and prolonged battery life. In recent years, the potential of connected and autonomous vehicles has grown significantly due to current technologies, enabling vehicle efficiency improvements [15,16] while maintaining high safety standards [17]. Connectivity is pivotal in enhancing vehicles' awareness of their surroundings and robustness in predicting external actions [18]. These improvements are crucial for improving vehicle performance in challenging conditions where sensors face limitations [19].

Literature Review

A few research works are presented in the literature on potential methods to leverage V2V communication in improving energy efficiency and reducing battery SOH degradation. The authors in [20] corroborated that an EV's energy consumption can be minimized at signalized intersections in city driving conditions if their speed profiles can be optimally controlled with an MPC framework, which exploits vehicle-to-infrastructure (V2I) communication, in comparison to manual, uninformed driving. However, this work did not exploit V2V communication and did not consider battery SOH degradation or maintaining a safe distance from the leading vehicle. An adaptive cruise control framework is presented in [21] to exploit V2V communication to maintain a constant distance between the Ego and the Leading vehicle but overlooking the optimal energy consumption of the Ego vehicle. The frameworks in the above-mentioned articles are designed for a fixed driving scenario, making them non-adaptive to varying driving scenarios. The optimizer governs the adaptability of the eco-driving feature, and neither dynamic programming nor Pontryagin's minimum principle-based optimizers can facilitate adaptability [22,23]. Reinforcement learning (RL)-based optimizers are widely accredited for their adaptability [24] to different driving conditions, and authors in [14,25] presented adaptive cruise control with eco-driving features for EVs to improve energy efficiency and ensure safe following distance.

Nevertheless, RL-based methods have the intrinsic drawback of substantial training and safety conformity [26]. Moreover, model-based RL approaches [14,25] need to learn the model of the traffic dynamics before prescribing optimal eco-driving control. An alternative solution, a data-driven predictive control, eliminates the need to learn a traffic dynamics model by leveraging historical data to inform control decisions [27]. While similar to

RL-based eco-driving control in its adaptability to varying driving scenarios, it necessitates a significant volume of data for accurate predictions.

Both linear [28] and non-linear [29] MPC frameworks have been proven to be suitable for real-time implementation of eco-driving-inspired adaptive cruise controls in NI real-time hardware [28] and dSpace MicroAutobox 1401 [29], respectively, and validating their battery life saving and energy saving capabilities, respectively. The efficacy of such eco-driving features and adaptive cruise control critically hinges upon the latency of V2V communication, which often hinders their real-world implementation. One approach to counter this issue is preparing a robust MPC framework against stochastic communication delays [30].

Looking at the strengths of V2V communication in designing an eco-driving feature for the adaptive cruise control module of the EV's VCU and identifying the drawbacks of the existing literature, the authors are inspired to enhance the capabilities of OACC. The proposed OACC will improve energy efficiency, reduce battery SOH degradation, and maintain safe inter-vehicular distance by optimally controlling the acceleration trajectory for a short-term future time window in the presence of stochastic delay within V2V communication. As shown in Figure 2, the fundamental idea of this intelligent feature is to consider the EV as an Ego vehicle and optimally control its acceleration trajectories for a short-term future time window by exploiting the Leading vehicle's position and speed through a linear MPC.

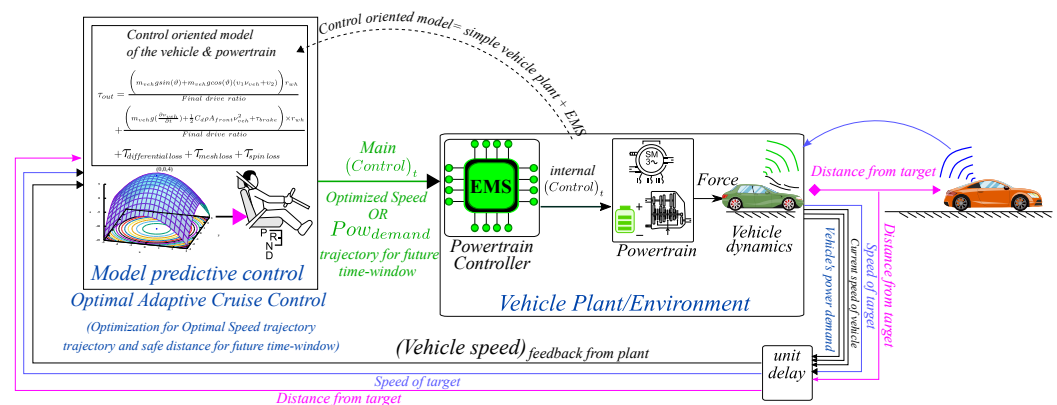


Figure 2. Concept of optimal speed trajectory planning with a linear MPC framework in connected vehicle environments.

Compared to the existing literature, this research article has the following contributions:

- Formulating a less computationally expensive MPC framework for solving the OACC problem;
- Fulfilling three objective simultaneously, i.e., energy efficiency, reducing battery SOH degradation, and maintaining safe inter-vehicular distance;
- Making the MPC framework robust against external disturbances such as sensory noise and communication delays.

The paper is organized as follows. The paper introduces the vehicle model in Section 2, providing a foundational understanding of the research context. Following this, Section 3 formulates the problem of optimizing the speed profile, setting the groundwork for the subsequent sections. Section 4 takes a closer look at the implementation of the MPC model, providing insights into how speed optimization is carried out. In Section 5, the paper presents simulation results and engages in detailed discussions related to these findings. Finally, the paper culminates in its concluding section, summarizing the work and drawing insights based on the research and its outcomes.

2. Forward Approach Electric Vehicle (EV) Modeling

This section will present the vehicle plant model, which serves as the foundational basis for implementing the proposed OACC. The model is designed to describe the longitudinal dynamics of a battery electric vehicle city car (2015 Chevy Spark) equipped with a single electric motor (EM), one inverter, and a single-gear transmission at the wheel level, as shown in Figure 3. Throughout this section, the BEV city car under consideration will be referred to as the *Ego* vehicle. The vehicle following a predefined driving cycle will be referred to as the *Leading* vehicle.

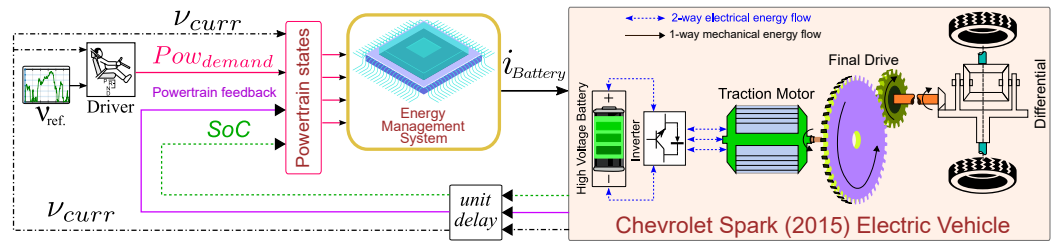


Figure 3. The simulation framework for a battery electric vehicle in Simulink® environment.

2.1. Longitudinal Dynamics

In this subsection, we provide the equations that describe the forward model for the longitudinal dynamics of the *Ego* vehicle. These equations are essential for understanding the interactions between the vehicle's speed, torque, and the various forces acting upon it. Equation (1) describes the electric motor torque demand from the driver, T_m , determined through a proportional–integral (PI) controller which commands it according to the error between the desired speed v_{dem} and the actual chassis speed v_{chas} . Additionally, the contribution due to resistance forces, such as aerodynamics, rolling, slope, and inertia, are taken into account into T_{loss} as follows:

$$T_m = (v_{dem} - v_{chas}) * K_p + \left[\int_0^t (v_{dem} - v_{chas}) dt \right] * K_i + T_{loss} \quad (1)$$

Once the torque demand at the motor level is determined, the torque acting at wheel level T_w can be evaluated. This calculation considers the final drive transmission efficiency η_{fd} and the final drive transmission ratio τ_{fd} and accounts for braking and accelerating. Calculation of T_w is given in Equation (2), as follows:

$$T_w = T_m * \eta_{fd}^{sign(T_w)} * \tau_{fd} \quad (2)$$

Once the torque at wheel level is computed, it is possible to evaluate the chassis's acceleration, speed, and position through Equation (3), integrating the \ddot{x} term once and integrating it twice, respectively.

$$M_{eq} \ddot{x} = \frac{T_w}{R} - F_{brk} - F_{res}, \quad (3)$$

where the vehicle equivalent mass (M_{eq}) considers the motor, final drive, and wheel inertias; R is the wheel radius; F_{brk} is the braking force; and F_{res} is the resistance force due to rolling, aerodynamics, and slope, as described in Equation (4).

$$F_{res} = \frac{1}{2} \cdot \rho_{air} \cdot A_{front} \cdot C_x \cdot v_{ch,actual}^2 + m_{vh} \cdot g \cdot \sin(\alpha) + m_{vh} \cdot g \cdot \cos(\alpha) \cdot (f_0 + f_1 \cdot v_{ch,actual}), \quad (4)$$

where $\dot{v}_{ch,actual} = \frac{C_0 + C_1 \cdot v_{ch,actual} + C_2 \cdot v_{ch,actual}^2}{M_{eq}}$. The first component is the aerodynamic resistance force, the second indicates the road-slope-induced resistance force, and the third represents the rolling force. All the parameters used for mathematically modeling vehicle dynamics are listed in Table 1.

Table 1. Definition of the parameters of vehicle’s dynamics-related formulas.

Parameter	Definition
K_p	Proportional factor of the PI controller
K_i	Integrator factor of the PI controller
η_{fd}	Final drive efficiency
τ_{fd}	Final drive transmission ratio
M_{eq}	Equivalent mass
R	Wheel radius
ρ_{air}	Air density
A_{front}	Projected vehicle frontal area
C_x	Longitudinal air resistance coefficient
α	Road slope
$f_0 \& f_1$	Road load coefficients
C_0, C_1, C_2	Cost-down coefficients

2.2. Battery Model

A battery model based on data from [31] has been implemented in the previously presented BEV architecture to ensure reliable and consistent results. This model simplifies the battery as a series and parallel connections of elementary cells. This representation includes a voltage generator representing the cell’s open circuit voltage (OCV) in series with a resistance representing the cell’s internal resistance. To match the energy storage performance of the actual Chevy Spark BEV, the cells from the paper were configured in 121 series and 22 in parallel. These cells are A123 26650 LiFePO₄ lithium-ion cylindrical cells with a nominal voltage of 3.3 V and a rated capacity of 2.5 Ampere-hours (Ah). To implement this model, some preliminary assumptions were made. First the elementary cell has been included as a voltage generator in series with an internal resistance considered adequate for assessing battery dynamics in this study. Then, it has been assumed that the BMS can maintain the temperature of the pack constant at 25 °C regardless of external temperature and load conditions. The internal resistance is also considered equally in both charging and discharging conditions. Lastly, uniform cell discharge/charge levels across the battery pack have been considered thanks to BMS working correctly.

2.3. State of Health Estimation Model

As outlined in [31], the attainable maximum capacity of a battery progressively diminishes as the it undergoes degradation. This, in turn, translates into a diminished range for the battery’s operation. Furthermore, the OCV declines and internal resistance increases due to the natural wear and aging of internal components (SOH decreases), as shown in Figure 4a,b where experimental data from battery fading test illustrated in [31] are considered.

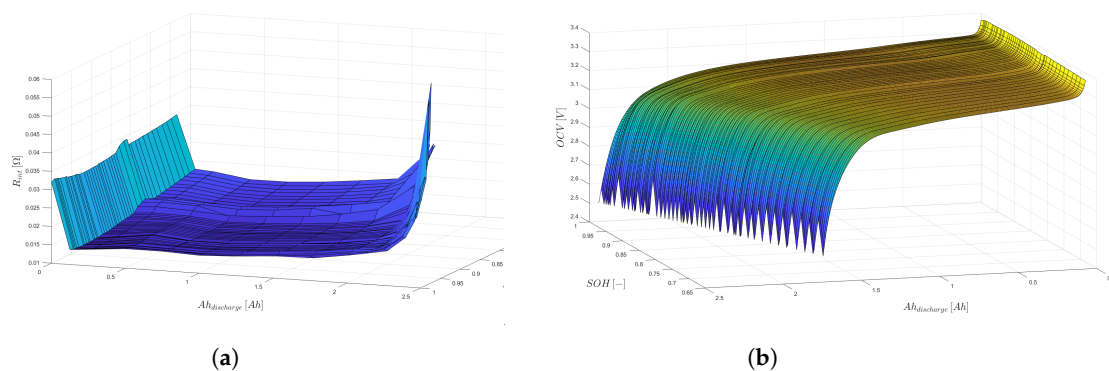


Figure 4. Characteristic contour plots of an A123 26650 LiFePO₄ lithium-ion cylindrical battery cell: (a) cell state-of-charge (SOC)–OCV relationship at different battery state of health (SOH) values; (b) cell SOC–internal relationship at different battery capacities.

Since directly measuring the SOH of a battery is not feasible, an analytical method with empirical fitting has been developed using a mathematical model exploiting the Arrhenius relation and a Coulomb counting method to estimate the current SOH of the battery. Equation (5) allows us to evaluate the cell capacity loss as a percentage:

$$Ah_{batt}\% = B(c) \cdot \exp - \frac{Af}{T} \cdot Ah_{tp}^z, \quad (5)$$

where $Ah_{batt}\%$ represents the cell capacity loss as a percentage and B is a pre-exponential factor determined through the experimental fitting of real data in [31]. Its values vary with the current C-rate, considering both calendar aging and wear due to battery usage. The pre-exponential factor values are tabulated in Table 2 below.

Table 2. Explanation of the entries of the SOH model.

Parameter	Unit of Measurement	Definition
Aging factor, A_f	K	$3814.7 - 44.6 \cdot c$
Power law factor, z	—	0.55
Battery temperature, T_{bat}	K	298.15
Empirical pre-exponential factor, $B(c)$	—	[21.681; 12.934; 15.512; 15.512]
C-rate, c	1/h	[2; 6; 10; 20]

Here c is the current C-rate (the ratio of the current to the nominate cell capacity $\frac{I}{C_{nominal}}$), A_f is the aging factor defined in this table, T represents the cell temperature (considered fixed at 25 °C), $Ah_{tp}(c, T)$ denotes the total Ampere-hours throughput considered for a specific C-rate and cell temperature, and z is an exponential factor set experimentally equal to 0.55.

To ascertain the battery's cycle life, we assume the EOL occurs when 20% of battery capacity is lost. By setting $Ah_{batt}\%$ to 20% and inverting equation (5), number of cycles the battery can withstand up to EoL for a given C-rate and cell temperature can be calculated through Equation (6):

$$N(c, T_{bat}) = \frac{Ah_{tp}(c, T_{bat})}{2 \cdot Ah_{batt}}, \quad (6)$$

where Ah_{batt} is the rated battery capacity evaluated in Ampere-hours, which for an A123 cell is 2.5 Ah. Once this variable has been evaluated, it is possible to evaluate the $SOH(t)$ at a specific instant ' t ' integrating into the equation over time, as shown in Equations (7) and (8), providing the output of the estimator block:

$$\dot{SOH}(c, T) = 0.2 \cdot \frac{c}{3600 \cdot N(c, T_{bat})} \quad (7)$$

$$SOH(t) = SOH_0 - \int_0^t \dot{SOH} \cdot d\tau \quad (8)$$

In this case, the state of health for the initial condition (SOH_0) is set to 1, indicating a new battery cell. After this block outputs the current SOH, it influences the cell's OCV and internal resistance. Subsequently, it enters the SOC estimator, which evaluates the SOC simply as the ratio between the cell's actual and maximum capacity, adjusting the second term to account for reduced energy storage capabilities due to degradation.

2.4. Simulation Setup

To establish a car-following simulation, which mathematically describes how vehicles follow one another on the road, the behavior of the leading vehicle to be followed must be selected. Two distinct driving cycles are employed to represent realistic scenarios: the Worldwide Harmonized Light Vehicles Test Cycle (WLTC), used in Europe, and the EPA cycle, utilized in the United States. This last cycle combines two sub-cycles: the Urban Dynamometer Driving Schedule (UDDS), simulating city driving conditions for testing

Light-Duty Vehicles (LDVs), and the Highway Fuel Economy Test (HWFET). These two cycles aim to encompass diverse driving scenarios, ensuring comprehensive testing and evaluation of the BEV model. Several realistic assumptions were made regarding the environmental setup for the model:

- Only two vehicles are present in the environment;
- No vehicles enter or exit the lane;
- Only longitudinal dynamics are examined and controlled;
- All types of road conditions, from urban roads to highways, are considered without accounting for traffic, focusing solely on the actions of the Leading vehicle;
- Information from the leading vehicle, including actual speed and position, is available through V2V or V2I communication or sensors, giving the possibility for the Leading and Ego vehicles to be either connected or not connected;
- Disturbances in the Leading vehicle's information are considered white noise with a specified maximum amplitude, accounting for sensor accuracy and communication delays.

In this scenario, the Ego vehicle's initial conditions are SOC = 95%, SOH = 1, $v_0 = 0$ (initial vehicle speed), and $x_0 = 0$ (initial position).

3. Formulating the Speed Profile Optimization Problem

In the following paragraph, we elaborate on the OACC problem, giving the basis for the implemented MPC strategy.

Optimal ACC Problem Formulation

The MPC requirements are multifaceted, encompassing the regulation of the vehicle's acceleration command with the overarching goals of minimizing energy consumption and positively impacting battery degradation. Simultaneously, the MPC aims to enhance comfort, maintain consistent travel time, and operate within stringent safety constraints. Achieving these objectives involves a strategic compromise in the relative distance and speed between vehicles, ensuring a dynamically adjusted minimum safe distance in accordance with the vehicle's speed. These goals are actualized through the utilization of data derived from vehicle-embedded sensors and facilitated by V2V and vehicle-to-everything (V2X) communication.

The control mechanism outlined in Equation (1) defines the longitudinal dynamics of the vehicle. In this formulation, the sole control input is the demanded vehicle speed, a parameter derived through the integration of the commanded acceleration. The instantaneous control input, denoted as $a_{command}$, adheres to the constraints of $Jerk_{max}$, confined within the following interval, as shown in Equation (9):

$$a_{command}(t) - Jerk_{max} \cdot d\tau < a_{command}(t+1) < a_{command}(t) + Jerk_{max} \cdot d\tau \quad (9)$$

This ensures a realistic and feasible range for the tested acceleration at each time step. Furthermore, the control design imposes constraints on the position and speed of the Ego vehicle concerning the Leading vehicle, as shown in Equation (10).

$$\begin{aligned} \Delta_{d_min} < \Delta_{distance} < \Delta_{d_max} \\ \Delta_{v_min} < \Delta_{speed} < \Delta_{v_max} \\ v_{ego} > 0 \end{aligned} \quad (10)$$

In the aforementioned formulation, $\Delta_{distance}$ denotes the disparity between the actual inter-vehicular distance and the desired distance. The desired distance is determined by considering a fixed time gap (h'_{ego}), and evaluating it based on the Ego vehicle's speed. These parameters are allowed to vary freely within a specified range, encompassing a lower bound to ensure a minimum safe distance and an upper bound beyond which the following is considered broken. The values of Δ_{d_min} , Δ_{d_max} , Δ_{v_min} , Δ_{v_max} , $Jerk_{max}$, and h_{ego} are furnished in Table 3.

Another constraint pertains to the speed factor, regulating the relative speed (Δ_{speed}) between the two vehicles and ensuring it stays within two designated values. Regarding the model’s ability to predict future actions, a crucial assumption is made regarding the state of the *Leading* vehicle: The *Leading* vehicle’s speed, obtained from sensors or connectivity, remains constant during the predictive horizons. This assumption is grounded in the aggressive WLTC cycle, where the maximum variation in one time step for peak speed values is merely 0.175 m/s, thereby validating its credibility.

Table 3. MPC controller parameter.

Parameters	Unit of Measurement	Values
$\Delta_{d_min}/\Delta_{d_max}$	m	0, 20
$\Delta_{v_min}/\Delta_{v_max}$	m/s	-10, 10
$Jerk_{max}$	m/s ²	4
h_{ego}	s	2.7

4. Solving the Speed Optimization Problem with Linear MPC

This section delves into each facet of the linear MPC architecture, elucidating the steps in solving the acceleration optimization problem. Figure 5 visually depicts the implementation of the concept in the Simulink® platform, encapsulating the *Ego* vehicle, the *Leading* vehicle, and the MPC controller.

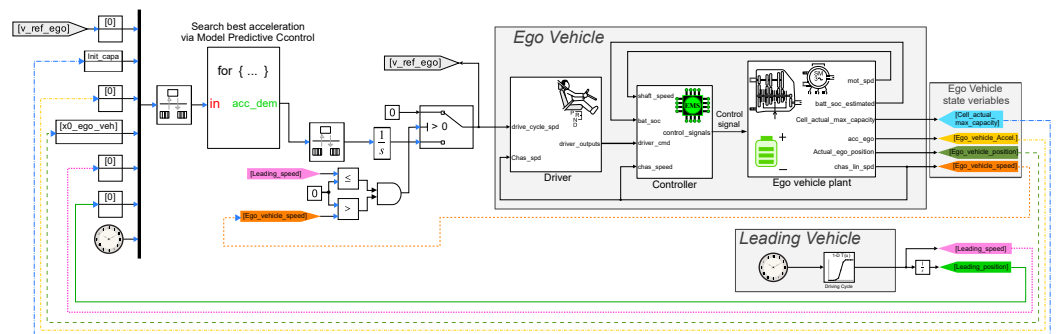


Figure 5. Implementation of the optimal speed trajectory planning in Simulink® platform.

4.1. Definition of Controller Inputs

The initial and pivotal step entails defining the inputs for the controller. Employing the Simulink® 2022a for iteration block to account for iterations, careful consideration is given to the inputs necessary for accurate future predictions. The variables incorporated into the input blocks encompass all the essential states of both the *Leading* and *Ego* vehicles. These states are critical for evaluating the cost function outlined in the subsequent section and are indispensable for simulating the linearized vehicle model within the controller block.

4.2. Acceleration for Loop

Upon entering the MPC block, a nested structure of two “For” loop blocks is employed. The external loop systematically tests various accelerations, while the internal loop assesses the optimal acceleration based on cost considerations over multiple time steps. To balance computational cost and result accuracy, the “For” loop employs a more complex architecture. Recognizing the vehicle’s feasibility limits related to jerk and aiming to reduce the number of iterations, a linear relation is utilized:

$$acc_{test} = acc_{min} + \frac{(acc_{max} - acc_{min}) * (iter_{actual} - iter_{min})}{iter_{max} - iter_{min}} \tag{11}$$

Equation (11) ensures that only feasible accelerations within the current *Ego* vehicle’s acceleration range are tested, thereby reducing the number of iterations, enforcing feasibility

limits, and enhancing comfort by limiting jerk values. However, avoiding an excessively narrow acceleration range is crucial to prevent impairment of the vehicle's following capability and divergence of the simulation.

4.3. Cost Function

In MPC, the cost function, denoted as J , is a mathematical function that assesses the cumulative performance of control inputs and system states over a finite prediction horizon N . It is formulated as the sum of individual cost terms, as shown below:

$$J = \sum_{k=1}^N L(x_k, u_k) \quad (12)$$

The state cost function $L(x_k, u_k)$ quantifies how desirable or undesirable a particular state (x_k) and control input (u_k) are at each time step k . For this application, key states include *Leading* vehicle speed ($\dot{x}_{leading}$), *Leading* vehicle position ($x_{leading}$), *Ego* vehicle speed (\dot{x}_{ego}) and vehicle position (x_{ego}), and *Ego* SOC (SOC_{ego}). The primary control action, u_k , is the commanded acceleration ($acc_{command}$). The central objective of the MPC is to determine the optimal control input u^* (in this case, acceleration) that minimizes the total cost J , while satisfying system dynamics and input/output constraint $u^* = argmin(J)$. In tailoring the cost function for our specific application, addressing requirements related to following capability and energy management is paramount. The designed total cost function J is formulated as follows:

$$J = \sum_{k=1}^N \left[\alpha \left(\frac{\Delta_{distance}}{\Delta_{d_max}} \right)^2 + \beta \left(\frac{\Delta_{speed}}{\Delta_{v_max}} \right)^2 + (1 - \alpha - \beta) \left(\frac{-\Delta_{SOC}}{\Delta_{SOC_max}} \right) \right] \quad (13)$$

Within this comprehensive cost function, three primary contributions are discerned, each focusing on specific control aspects: The component $\Delta_{distance}$ is pivotal in maintaining the vehicle within the desired distance range, considering distance errors at future time steps. The parameter α provides a mechanism for adjusting the weight allocated to these desired distance constraints. Additionally, Δ_{d_max} signifies the maximum allowable distance, serving to normalize the distance term. The inclusion of the square term enables the consideration of both positive and negative deviations as detrimental, contributing to a comprehensive evaluation. The key variable in this factor is defined as

$$\Delta_{distance} = [(x_{ego} - x_{leading}) - (h_{ego}\dot{x}_{ego} + s_{ego_0})]^{k+1} \quad (14)$$

Breaking this down, the first difference represents the vehicle distance at the next step, aligning it with the desired distance based on the vehicle's speed shown by the second term. Here, s_{ego_0} signifies the desired distance when both vehicles are stationary, set at 5 m. Δ_{speed} enables the *Ego* vehicle to conform, to a varying degree, to a predefined vehicle speed profile. Similar to the $\Delta_{distance}$ term, a normalization process is implemented to adapt to the maximum speed variation prescribed between the two vehicles. The introduction of the square term serves the same purpose as in the preceding case, allowing consideration of both positive and negative variations as impactful. The parameter β assumes the role of the weighting factor, influencing the overall impact of this contribution in the cost function.

$$\Delta_{speed} = [\dot{x}_{ego} - \dot{x}_{leading}]^{k+1} \quad (15)$$

where the $\Delta_{SOC} = (SOC^{k+1} - SOC^k)$ term encapsulates the difference between the *Ego* vehicle's state of charge (SOC) in the subsequent time step and its current state.

The weighting factor for this term is designated as $(1 - \alpha - \beta)$ to establish a hierarchy in cost assignment compared to the other two components. This formulation ensures that an increase in the weight of a factor results in a proportionate rise in cost, emphasizing its impact on the overall cost function. Like the distance and speed terms, the term Δ_{SOC_max} acts as a normalization factor. In contrast to the squared terms applied to distance and

speed, the SOC factor remains unsquared. This decision stems from acknowledging that its negative effect should be considered exclusively when the SOC decreases, not in both directions. Thus, a minus sign is introduced into the function to underscore higher costs for actions causing substantial negative variations in SOC. The weight parameters were strategically selected to prioritize energy consumption while assigning relatively lower importance to speed and distance factors, while always ensuring safety constraints are met. This balance permits more extensive variations in speed and distance from the nominal values, promoting smoother velocity profiles while still providing adequate following capability. Specifically, α was configured to a value of 0.15, and β was set to 0.05 for these reasons.

4.4. Linearized Vehicle Model

The implemented strategy establishes a linear relationship between vehicle states and the control variable, significantly reducing simulation costs. Assuming precise replication of the imposed driving cycle by the *Ego* plant, the future *Ego* vehicle speed, position, and acceleration can be linearly evaluated based on the command input. A different approach has been required for the correlation between command input and *Ego* battery SOC.

In this case, a linear relation between command acceleration and the ratio $\frac{\text{cellcurrent}}{\text{vehiclespeed}}$ has been found through multiple simulations. The choice of this specific ratio has been dictated by the dependence of the cell current on the acceleration and the current vehicle speed. This approach has enabled a significant simplification of the vehicle model, facilitating the estimation of all required vehicle states and allowing for the computation of the cost function multiple times within the predictive horizon.

4.5. Linear MPC with Predictive Horizon = 10 and Control Horizon = 2

Having undertaken these activities to drastically reduce computational costs, the final step involves finding the optimal balance between performance and computational efficiency. Through multiple simulations, the optimal configuration was identified with a predictive horizon (P.H.) of 10 and a control horizon (C.H.) of 2. In this scenario, the prediction horizon is sufficiently large to ensure a smooth profile without an excessively long horizon, which could lead to incorrect predictions. This is crucial, especially considering the assumption of a constant *Leading* vehicle speed, preventing overshoot in the *Ego* vehicle's actions during transitions from braking to accelerating and vice versa.

Adjusting the predictive horizon (P.H.) is achieved by increasing the number of iterations for the internal loop, whereas controlling the control horizon (C.H.) is a different process. The control horizon represents the time or states in the future for which the controller actively computes and applies control inputs to the system. The solution implemented here involves a control horizon (C.H.) greater than 1, specifically set to 2, operating with constant acceleration during this period.

To predict values every two time steps and act on the plant accordingly in the subsequent two time steps, a Simulink® 2022a 'Rate Transmission' block was incorporated. This block adjusts the sampling frequency of its output, modifying the operational response of the subsequent blocks. Placing this block before the MPC controller and setting the output sampling frequency to half of the simulation frequency ensures results every two simulation time steps.

Upon exiting the MPC controller block, the rest of the Simulink® model must revert to working with the normal sampling frequency. Therefore, another 'Rate Transmissio' block with an output frequency equal to the simulation frequency was introduced. Given that the input to this block is generated every two simulation time-steps, the remaining time step is kept constant, equal to the last output value. This architecture enables the prediction of a single commanded acceleration while acting on two time-steps, significantly reducing computational costs and spreading MPC predictions over two time-steps.

5. Simulation Results and Discussion

This section presents the simulation results of the *Ego* vehicle in comparison to the *Leading* vehicle following the WLTC and EPA driving cycles in Sections 5.1 and 5.2, respectively. The effectiveness of the proposed OACC was evaluated in terms of energy efficiency, battery durability, and driver's comfort.

5.1. WLTC-Based Results

In this case, the *Leading* vehicle is following the WLTC cycle, and the *Ego* vehicle is receiving continuous information about the *Leading* vehicle's speed and position. The VCU of the *Ego* vehicle, featuring the MPC, optimally plans its vehicle speed trajectory. The speed trajectories of the two vehicles are compared in Figure 6.

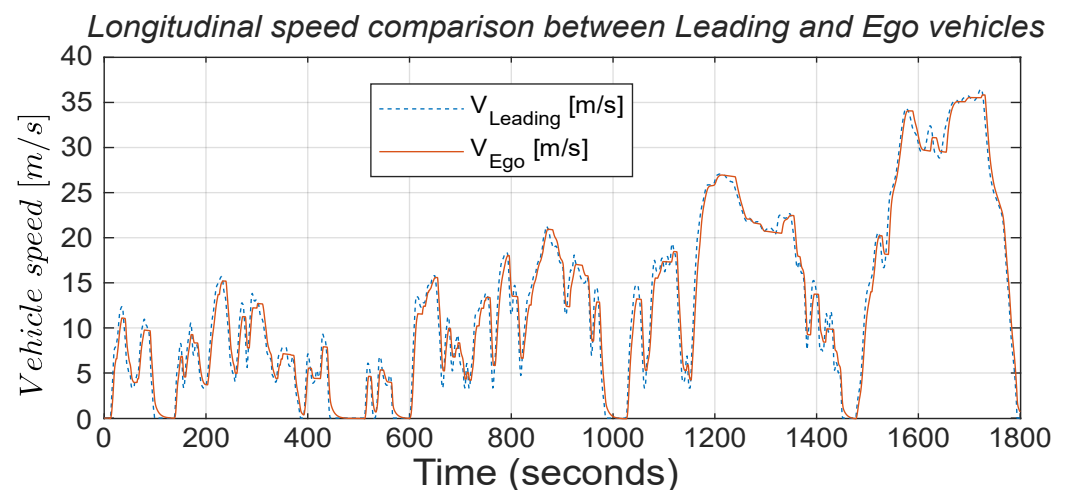


Figure 6. WLTC longitudinal speed plot LMPC PH = 10, CH = 2.

The acceleration command exhibits significantly less oscillation, with considerable reductions in all peaks due to the application of OACC, as shown in Figure 7a. The “continuous” and “dashed” lines represent the *Ego* and the *Leading* vehicles' acceleration profiles, respectively. During deceleration, a smoothing effect is possible due to the soft constraint on distance, which allows for larger variations. This is possible thanks to the distance constraint, which prevents the speed from rapidly reaching zero to approach the desired distance when the vehicle is stationary. This allows for a gradual reduction in speed until reaching a distance of 5 m.

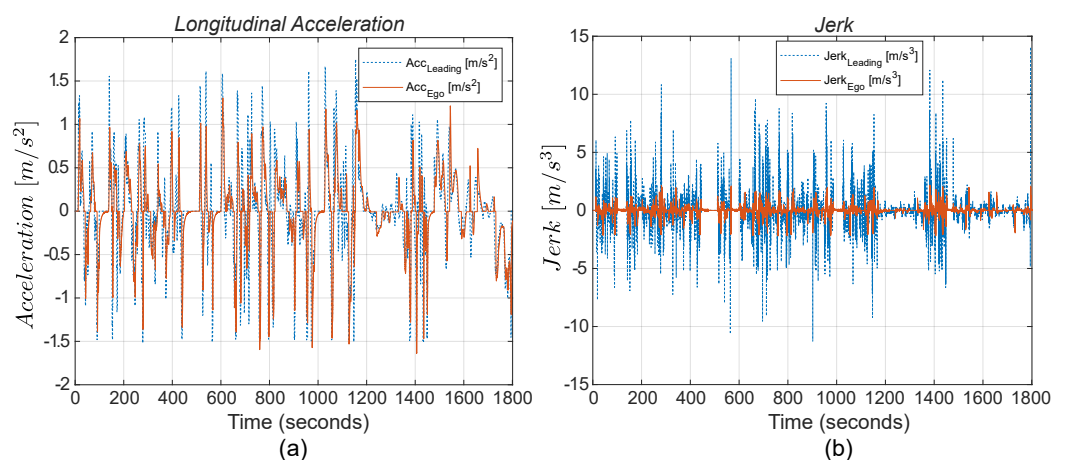


Figure 7. WLTC longitudinal acceleration (a) and jerk (b) plots LMPC PH = 10, CH = 2.

This approach provides a substantial reduction in power requests. Furthermore, in terms of comfort, jerk values are greatly reduced in all conditions, more than halved, as shown in Figure 7b, indicating that the controller operates more effectively and smoothly.

Examining the speed profiles in Figure 6, it is evident that the initial objective set at the beginning has been successfully achieved. The *Ego* vehicle, predicting future vehicle behavior of the *Leading* vehicle, optimizes its trajectory, smooths its speed profile, and avoids the oscillations present in the behavior of the *Leading* vehicle. All speed peaks are diminished, and the vehicle approaches zero speed more smoothly, sometimes even avoiding stops when the *Leading* vehicle comes to a halt for the previously mentioned reason. In many instances, the *Leading* vehicle experiences rapid positive and negative speed changes, but our *Ego* vehicle effectively smooths them out, exhibiting nearly linear behavior. Moreover, the inter-vehicle distance is smartly managed by the *Ego* vehicle's OACC, varying as much as needed within the desired interval without ever falling below the safety distance or exceeding the maximum limit, as shown in Figure 8. This figure shows how effectively the OACC varies the inter-vehicular distance within the boundaries set between a safe distance to the maximum distance to optimally regulate the vehicle's acceleration.

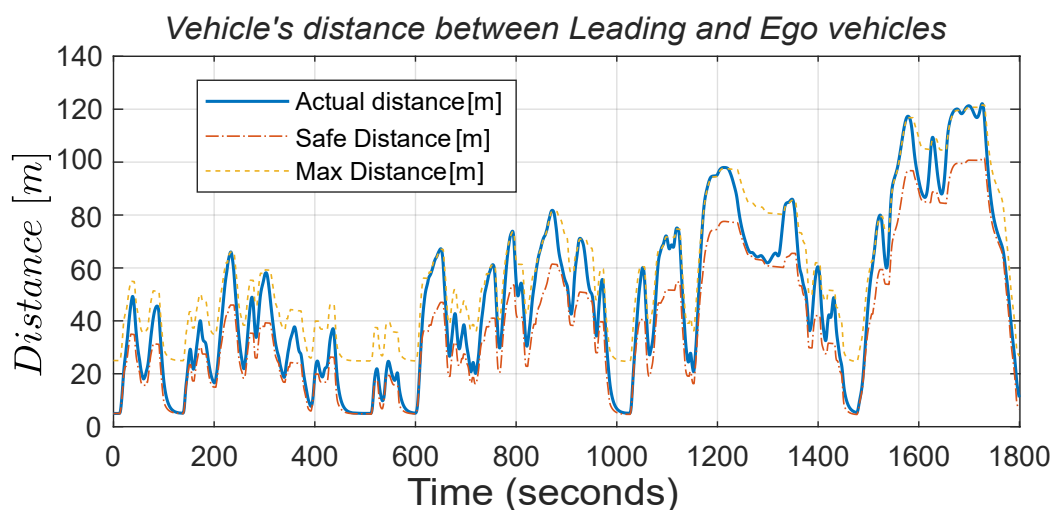


Figure 8. Vehicle distance plot LMPC PH = 10, CH = 2.

The improvements achieved with this approach are more significant, with a 3.7% reduction in energy consumption and a 9.7% reduction in battery SOH degradation, as shown in Figure 9 and Figure 10, respectively. The respective battery SOC trajectories indirectly measure the comparison between energy consumption for the *Ego* and *Leading* vehicles, whereas the reduction in SOH degradation in the *Ego* vehicle is directly measured by comparing the SOH trajectories for two vehicles in Figure 10.

These values are primarily due to the improvements obtained in Figure 7a with a 6.5% reduction in maximum acceleration, indicating a decrease in power demand. Regarding comfort, Figure 7b shows an 81% reduction in jerk peaks, ensuring a substantial improvement for passengers. These improvements are achieved while keeping travel time almost constant, with a difference of only 5 s for the same distance traveled.

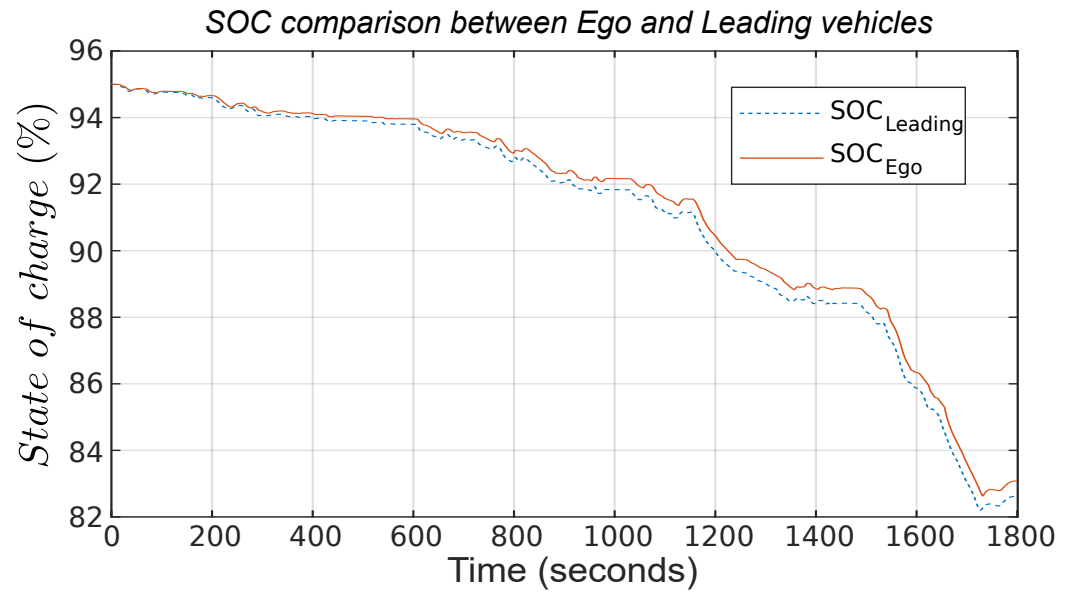


Figure 9. Energy consumption reduction in EV due to optimal adaptive cruise control.

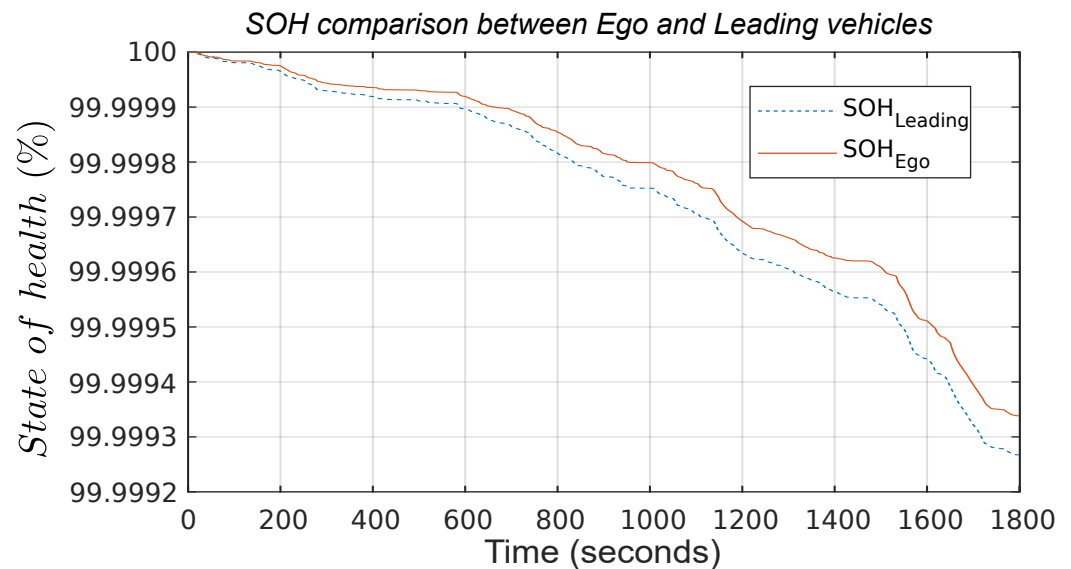


Figure 10. Reduction in battery health degradation due to optimal adaptive cruise control.

5.2. EPA-Based Results

All these experiments were replicated for the EPA cycle, showcasing the ability to improve energy efficiency and battery durability performances in a different driving scenario. Figures 11 and 12 show the comparison between the vehicles regarding vehicular acceleration and jerk, respectively. In this case, given the less aggressive nature of the cycle, the improvements are naturally more minor but still substantial. Since these experimental charts do not provide additional information beyond what has been explained, only two figures illustrating speed smoothing are compared to the results following a *Leading* vehicle, ensuring completeness. Even for this cycle, all the previously stated findings are reaffirmed, with a significant 7.6% reduction in battery SOH degradation and a 2.8% reduction in energy consumption.

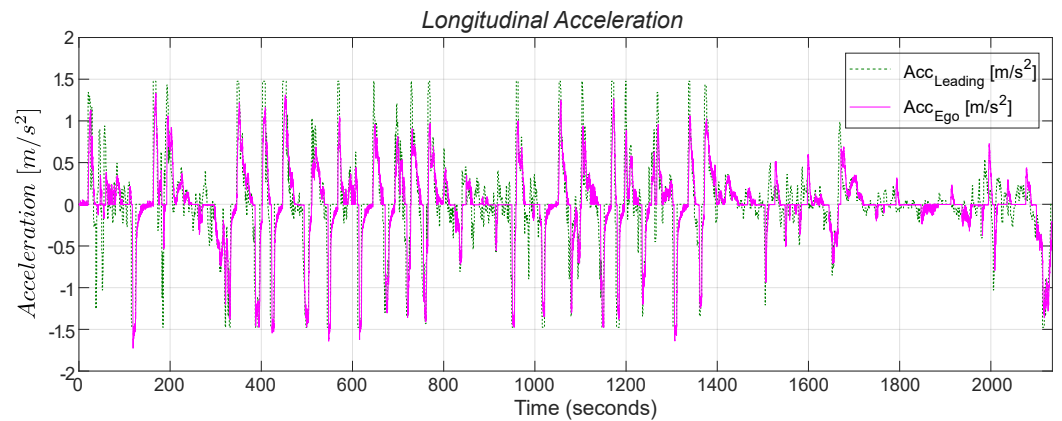


Figure 11. EPA longitudinal acceleration with LMPC PH = 10, CH = 2.

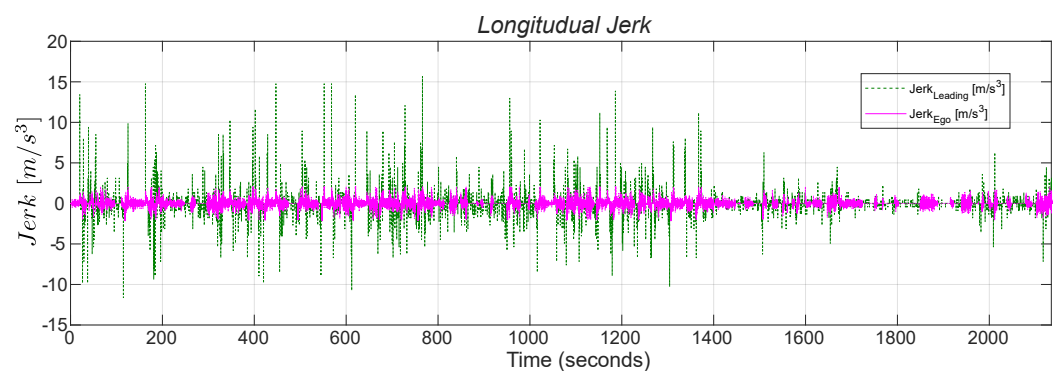


Figure 12. EPA longitudinal jerk with LMPC PH = 10, CH = 2.

Table 4 comprehensively furnishes all metrics of improvements resulting from the OACC for the *Ego* vehicle under WLTC and EPA cycles.

Table 4. Effectiveness of optimal speed trajectory planning enabled through V2V communication for EVs.

Comparison Metrics	WLTC Cycle	EPA Cycle
Energy consumption reduction [%]	3.7	2.8
Reduction in battery SOH degradation [%]	9.7	7.6
Peak acceleration reduction [%]	6.5	4.8
Peak jerk reduction [%]	81	74.5

5.3. Robustness Analysis: Noise and Delay Influence

To enhance the realism of the simulation, we considered incorporating noise and data delays in the Leading vehicle's information. We incorporated two simple blocks into the input for Leading vehicle speed and Leading vehicle position to introduce these external disturbances: a delay block and band-limited white noise. Since our application is non-safety-related, we used 5G cellular network technology for communication and a specific radar, LLR4 [3], commonly used in vehicle applications.

Given a simulation time-step of 100 ms in Simulink®, the minimum delay we could have implemented is at least that value. As outlined in [3], the delays associated with these technologies are notably lower:

- The long-range radar has a cycle time of 60 ms, indicating how frequently the sensor collects and processes data or updates its measurements.
- Average latency values, representing the delay or lag in data transmission between a sender and receiver, for specific countries are 32 ms for the United States (US) and

37 ms for Italy. While these values are averages and can vary by country, they provide a helpful reference, especially since they are lower than the sensor-induced delay.

This presents a situation where the implemented delay exceeds the actual delay, resulting in an overestimation of the disturbance.

Within one time step, assuming worst-case scenarios with maximum speeds in the WLTC, the speed variation is approximately 0.175 m/s, and the distance travelled is around 3.6 m. Given these values, we expect practically negligible variations in the speed profile and more significant changes in relative distance, as shown in Figure 13a. Particularly with respect to distance values, the *Ego* vehicle's controller consistently receives delayed information, effectively acting as if it were one time step behind. This discrepancy causes the actual accurate distance to be poorly managed, leading to unnecessary increases in the gap from the *Leading* vehicle at each moment, resulting in the vehicle being out of the upper bound limit. While this is almost imperceptible in speed, it is more noticeable in the relative distance. The phenomenon is illustrated in Figure 13b for the WLTC cycle.

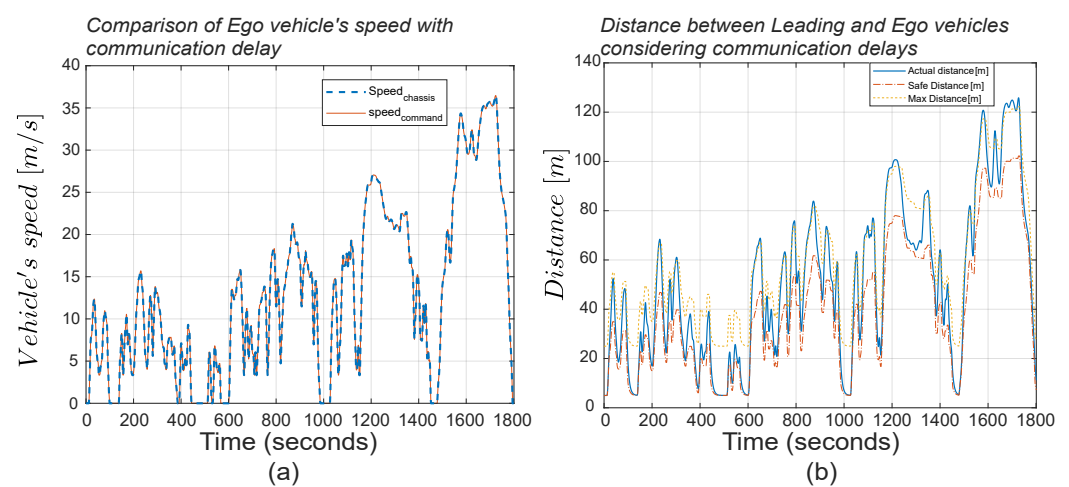


Figure 13. Effect of communication delay in operation and optimal adaptive cruise control's effectiveness. Effect of communication delay on the (a) vehicle's speed trajectory and (b) distance between *Ego* and *Leading* vehicles.

This behavior has minimal influence on the results. The SOC and SOH remain practically the same because the MPC operates as precisely as before, and the effect on distance goes unnoticed since the controller continuously considers the delayed information it receives. The simulation results on the EPA cycle with such disturbances and communication delays demonstrate a similar pattern. The second aspect that requires consideration is the presence of noise in the acquired information. Due to their nature, sensors inherently possess some degree of error in their measurements, leading to variations from the nominal values. This variation is precisely what sensor accuracy describes. For instance, ref. [3] indicates that the speed and distance measuring error achievable with the described long-range radar are approximately ± 0.11 m/s and ± 0.12 m, respectively.

Given this information, we introduced white noise with an amplitude within this specific range and a frequency equal to the simulation frequency (10 Hz) into our input signals. The addition of this noise has a more significant impact compared to the introduction of communication delays. This is because noise introduces oscillations in the commanded acceleration, which, even if to a small extent, deteriorates performance. Consequently, this effect results in a decrease in performance compared to improvements without noise, amounting to -2.17% of 3.7% for SOC and -2.3% of 9.7% for SOH improvements. These values are obtained when simulating a WLTC. However, the decrease is nearly the same for the EPA, with -2.78% for SOC and -2.4% for SOH. This is because its detrimental impact is independent of speed, unlike the delay.

6. Conclusions

The presented OACC is a valid solution for reducing battery health degradation and energy consumption in EVs by optimally and dynamically controlling vehicle acceleration and reducing peak power requests. The OACC decreases the energy consumption of a simulated passenger EV by as much as 3.7% and reduces battery health degradation by as much as 9.7% while always maintaining a safe inter-vehicle distance. Simply acting at the software level, the MPC can be easily integrated into any powertrain architecture with an autonomous driving level equal to 1, enforcing its broad applicability in the current automotive industry. Moreover, the proposed OACC's performance is promising, considering it is designed to be as light as possible, especially in more aggressive driving scenarios where its effect is more evident. As further analysis, the controller has been tested under realistic disturbance and scenarios with delayed V2V communication, showing excellent robustness and confirming its effectiveness and practicability. The real-time hardware-in-the-loop validation of the proposed OACC is planned as a future work. In summary, the OACC controller proposes an innovative architecture to address current critical automotive challenges, with promising results, highlighting its potential for widespread adoption and positive impact on the electric vehicle landscape. As the possibility of leveraging V2V communication in reshaping the EMS and adaptive cruise control frameworks is increasing, this research will motivate future scholars to investigate the effectiveness of OACC in traffic situations with signalized intersections and different highway driving conditions.

Author Contributions: Conceptualization, C.F. and A.B. (Atriya Biswas); Methodology, C.F.; Formal analysis, C.F.; Investigation, C.F.; Resources, M.M.; Data curation, C.F. and M.M.; Writing—original draft, C.F.; Writing—review & editing, A.B. (Atriya Biswas) and M.M.; Supervision, A.B. (Atriya Biswas), A.B. (Angelo Bonfitto) and A.E.; Project administration, A.B. (Atriya Biswas); Funding acquisition, A.E. All authors have read and agreed to the published version of the manuscript.

Funding: This research is supported, in part, thanks to funding from the Natural Sciences and Engineering Research Council of Canada (NSERC, grant number: 531565913); the NSERC Industrial Research Chair in Electrified Powertrains, Canada; and the Canada Research Chair in Transportation Electrification and Smart Mobility.

Data Availability Statement: The original contributions presented in the study are included in the article, further inquiries can be directed to the corresponding author.

Acknowledgments: The authors would like to thank Hao Wang and Junran Chen (PhD students at McMaster University) for their help in developing the electric vehicle modeling and battery state-of-health degradation modeling.

Conflicts of Interest: The authors declare no conflict of interest. The funders had no role in the design of the study; in the collection, analyses, or interpretation of data; in the writing of the manuscript; or in the decision to publish the results.

References

1. IEA. *Global CO₂ Emissions from Transport by Sub-Sector in the Net Zero Scenario, 2000–2030*; IEA: Paris, France, 2023.
2. IEA. *Global EV Outlook 2023: Catching Up with Climate Ambitions*; IEA: Paris, France, 2023.
3. Chu, Y.; Cui, H. *Annual Update on the Global Transition to Electric Vehicles: 2022*; The International Council on Clean Transportation: San Francisco, CA, USA, 2023.
4. IEA. *Electric Car Sales, 2016–2023*; IEA: Paris, France, 2023.
5. Chen, A.; Zhang, X.; Zhou, Z. Machine learning: Accelerating materials development for energy storage and conversion. *InfoMat* **2020**, *2*, 553–576. [[CrossRef](#)]
6. Anselma, P.G.; Biswas, A.; Belingardi, G.; Emadi, A. Rapid assessment of the fuel economy capability of parallel and series-parallel hybrid electric vehicles. *Appl. Energy* **2020**, *275*, 115319. [[CrossRef](#)]
7. Anselma, P.G.; Biswas, A.; Bruck, L.; Amirfarhangi Bonab, S.; Lempert, A.; Roeleveld, J.; Madireddy, K.; Rane, O.; Wasacz, B.; Belingardi, G.; et al. Accelerated Sizing of a Power Split Electrified Powertrain. *SAE Int. J. Adv. Curr. Pract. Mobil.* **2020**, *2*, 2701–2711. [[CrossRef](#)]
8. Louback, E.; Biswas, A.; Machado, F.; Emadi, A. A review of the design process of energy management systems for dual-motor battery electric vehicles. *Renew. Sustain. Energy Rev.* **2024**, *193*, 114293. [[CrossRef](#)]

9. Taggart, J. Ambient temperature impacts on real-world electric vehicle efficiency & range. In Proceedings of the 2017 IEEE Transportation Electrification Conference and Expo (ITEC), Chicago, IL, USA, 22–24 June 2017; pp. 186–190. [\[CrossRef\]](#)
10. Ou, S. Estimate long-term impact on battery degradation by considering electric vehicle real-world end-use factors. *J. Power Sources* **2023**, *573*, 233133. [\[CrossRef\]](#)
11. Etxandi-Santolaya, M.; Canals Casals, L.; Corchero, C. Extending the electric vehicle battery first life: Performance beyond the current end of life threshold. *Heliyon* **2024**, *10*, e26066. [\[CrossRef\]](#)
12. Karunathilake, D.; Vilathgamuwa, M.; Mishra, Y.; Farrell, T.W.; Choi, S.S. Capacity Loss Reduction using Smart-Battery Management System for Li-ion Battery Energy Storage Systems. In Proceedings of the 2020 IEEE 29th International Symposium on Industrial Electronics (ISIE), Delft, Netherlands, 17–19 June 2020; pp. 997–1002. [\[CrossRef\]](#)
13. Lin, Q.; Wang, J.; Xiong, R.; Shen, W.; He, H. Towards a smarter battery management system: A critical review on optimal charging methods of lithium ion batteries. *Energy* **2019**, *183*, 220–234. [\[CrossRef\]](#)
14. Lee, H.; Kim, K.; Kim, N.; Cha, S.W. Energy efficient speed planning of electric vehicles for car-following scenario using model-based reinforcement learning. *Appl. Energy* **2022**, *313*, 118460. [\[CrossRef\]](#)
15. Michel, P.; Karbowski, D.; Rousseau, A. Impact of Connectivity and Automation on Vehicle Energy Use. In Proceedings of the SAE 2016 World Congress and Exhibition, Detroit, MI, USA, 12–14 April 2016. [\[CrossRef\]](#)
16. Othman, B.; De Nunzio, G.; Sciarretta, A.; Di Domenico, D.; Canudas-de Wit, C. Connectivity and Automation as Enablers for Energy-Efficient Driving and Road Traffic Management. In *Handbook of Climate Change Mitigation and Adaptation*; Lackner, M., Sajjadi, B., Chen, W.Y., Eds.; Springer International Publishing: Cham, Switzerland, 2022; pp. 2337–2376. [\[CrossRef\]](#)
17. Abraham, A.; Nagavarapu, S.C.; Prasad, S.; Vyas, P.; Mathew, L.K. Recent Trends in Autonomous Vehicle Validation Ensuring Road Safety with Emphasis on Learning Algorithms. In Proceedings of the 2022 17th International Conference on Control, Automation, Robotics and Vision (ICARCV), Singapore, 11–13 December 2022; pp. 397–404. [\[CrossRef\]](#)
18. Ersal, T.; Kolmanovsky, I.; Masoud, N.; Ozay, N.; Scruggs, J.; Vasudevan, R.; Orosz, G. Connected and automated road vehicles: State of the art and future challenges. *Veh. Syst. Dyn.* **2020**, *58*, 672–704. [\[CrossRef\]](#)
19. Sinha, N. Emerging Technology Trends in Vehicle-to-Everything Connectivity. In Proceedings of the 2019 Wireless Telecommunications Symposium (WTS), New York, NY, USA, 9–12 April 2019; pp. 1–12. [\[CrossRef\]](#)
20. Qi, X.; Barth, M.J.; Wu, G.; Boriboonsomsin, K.; Wang, P. Energy Impact of Connected Eco-driving on Electric Vehicles. In *Road Vehicle Automation 4*; Meyer, G., Beiker, S., Eds.; Springer: Cham, Switzerland, 2018; pp. 97–111.
21. Hattori, M.; Fujimoto, H. Basic Idea of Quadrant Dynamic Programming for Adaptive Cruise Control to Create Energy Efficient Velocity Trajectory of Electric Vehicle. In Proceedings of the 2020 IEEE 16th International Workshop on Advanced Motion Control (AMC), Kristiansand, Norway, 14–16 September 2020; pp. 29–33. [\[CrossRef\]](#)
22. Ozatay, E.; Onori, S.; Wollaeger, J.; Ozguner, U.; Rizzoni, G.; Filev, D.; Michelini, J.; Di Cairano, S. Cloud-Based Velocity Profile Optimization for Everyday Driving: A Dynamic-Programming-Based Solution. *IEEE Trans. Intell. Transp. Syst.* **2014**, *15*, 2491–2505. [\[CrossRef\]](#)
23. Abbas, H.; Kim, Y.; Siegel, J.B.; Rizzo, D.M. Synthesis of Pontryagin’s Maximum Principle Analysis for Speed Profile Optimization of All-Electric Vehicles. *J. Dyn. Syst. Meas. Control.* **2019**, *141*, 071004. [\[CrossRef\]](#)
24. Biswas, A.; Anselma, P.G.; Emadi, A. Real-Time Optimal Energy Management of Multimode Hybrid Electric Powertrain With Online Trainable Asynchronous Advantage Actor–Critic Algorithm. *IEEE Trans. Transp. Electrif.* **2022**, *8*, 2676–2694. [\[CrossRef\]](#)
25. Lee, H.; Kim, N.; Cha, S.W. Model-Based Reinforcement Learning for Eco-Driving Control of Electric Vehicles. *IEEE Access* **2020**, *8*, 202886–202896. [\[CrossRef\]](#)
26. Biswas, A.; Acquarone, M.; Wang, H.; Miretti, F.; Misul, D.A.; Emadi, A. Safe Reinforcement Learning for Energy Management of Electrified Vehicle with Novel Physics-Informed Exploration Strategy. *IEEE Trans. Transp. Electrif.* **2024**. [\[CrossRef\]](#)
27. Wang, J.; Zheng, Y.; Dong, J.; Chen, C.; Cai, M.; Li, K.; Xu, Q. Implementation and Experimental Validation of Data-Driven Predictive Control for Dissipating Stop-and-Go Waves in Mixed Traffic. *IEEE Internet Things J.* **2024**, *11*, 4570–4585. [\[CrossRef\]](#)
28. Pan, C.; Zhang, C.; Wang, J.; Liu, Q. Adaptive Cruise Control Strategy for Electric Vehicles Considering Battery Degradation Characteristics. *Appl. Sci.* **2023**, *13*, 4553. [\[CrossRef\]](#)
29. Bertoni, L.; Guanetti, J.; Basso, M.; Masoero, M.; Cetinkunt, S.; Borrelli, F. An adaptive cruise control for connected energy-saving electric vehicles. *IFAC-PapersOnLine* **2017**, *50*, 2359–2364. [\[CrossRef\]](#)
30. Gao, Y.; Wang, Z.; Fang, C.; Luo, C.; You, S. Optimal Connected Cruise Control Design with Stochastic Communication Delays. In Proceedings of the 2019 International Conference on Internet of Things (iThings) and IEEE Green Computing and Communications (GreenCom) and IEEE Cyber, Physical and Social Computing (CPSCom) and IEEE Smart Data (SmartData), Atlanta, GA, USA, 14–17 July 2019; pp. 756–760. [\[CrossRef\]](#)
31. Anselma, P.G.; Kollmeyer, P.; Lempert, J.; Zhao, Z.; Belingardi, G.; Emadi, A. Battery state-of-health sensitive energy management of hybrid electric vehicles: Lifetime prediction and ageing experimental validation. *Appl. Energy* **2021**, *285*, 116440. [\[CrossRef\]](#)

Disclaimer/Publisher’s Note: The statements, opinions and data contained in all publications are solely those of the individual author(s) and contributor(s) and not of MDPI and/or the editor(s). MDPI and/or the editor(s) disclaim responsibility for any injury to people or property resulting from any ideas, methods, instructions or products referred to in the content.